







Background-oriented schlieren imaging of flow around a circular cylinder at low Mach numbers

Hannes Stadler¹  · André Bauknecht²  · Silvan Siegrist¹  · Robert Flesch¹  ·
C. Christian Wolf²  · Nils van Hinsberg³ · Markus Jacobs⁴ 

Received: 10 March 2017 / Revised: 5 July 2017 / Accepted: 7 July 2017 / Published online: 2 August 2017
© Springer-Verlag GmbH Germany 2017

Abstract The background-oriented schlieren (BOS) imaging method has, for the first time, been applied in the investigation of the flow around a circular cylinder at low Mach numbers ($M < 0.1$). The measurements were conducted in the high pressure wind tunnel, Göttingen, with static pressures ranging from 0.1 MPa to 6.0 MPa and covered a range of the Reynolds numbers of $0.1 \times 10^6 \leq Re \leq 6.0 \times 10^6$. Even at ambient pressure and the lowest Reynolds number investigated, density gradients associated with the flow around the cylinder were recorded. The signal-to-noise ratio of the evaluated gradient field improved with increasing stagnation pressure. The separation point could easily be identified with this non-intrusive measurement technique and corresponds well to simultaneous surface pressure measurements. The resulting displacement field is in principle of qualitative nature as the observation angle was parallel to the cylinder axis only in a single point of the recorded images. However, it has been possible to integrate the density field along the surface of the cylinder by successive imaging at incremental angular positions around the cylinder. This density distribution has been found to agree well with the pressure measurements and with potential theory where appropriate.

1 Introduction

The background-oriented schlieren (BOS) method, which has simultaneously been developed by Dalziel et al. (2000) and Raffel et al. (2000) is nowadays commonly used for the visualisation of density gradients, which occur in thermal flows (Tokgoz et al. 2012; Stadler et al. 2017), compressible vortex flows (Kindler et al. 2007; Bauknecht et al. 2014), or jet flows (van Hinsberg and Rösgen 2014). The BOS method is usually preferred over classical schlieren setups when the object under investigation is very large or when, for other reasons like a limited optical access or outdoor investigations, a classical laboratory schlieren setup is not feasible. A comprehensive review on the development and applications of BOS has been given by Raffel (2015).

Schlieren methods in general are very sensitive even to small density gradients. Nevertheless, the BOS method has not yet been applied to flows, which are typically considered isothermal and incompressible at the same time. In the current investigation it is shown that BOS is also applicable in visualising density gradients caused by the flow around a cylinder at low Mach numbers ($M < 0.1$) and at isothermal boundary conditions. For demonstration purposes, a well-studied case of 2D flow across a smooth circular cylinder has been studied here at a range of Reynolds numbers of $0.1 \times 10^6 < Re < 6.0 \times 10^6$.

Coutanceau and Defaye (1991) have gathered a comprehensive compilation of studies dealing with the visualisation of cylinder flows, but none of them investigate flows at high Reynolds numbers and low Mach numbers at the same time. The closest case is Rodriguez (1984), who used shadowgraph and schlieren imaging at $Re = 0.5 \times 10^6$ and $0.4 < M < 0.85$. More recently, Kakade et al. (2010) have used schlieren imaging for the investigation of vortex shedding of a slightly heated cylinder at low Reynolds numbers.

✉ Hannes Stadler
hannes.stadler@dlr.de

¹ Institute of Solar Research, German Aerospace Center (DLR), 52428 Jülich, Germany

² Institute of Aerodynamics and Flow Technology, German Aerospace Center (DLR), 37073 Göttingen, Germany

³ Institute of Aeroelasticity, German Aerospace Center (DLR), 37073 Göttingen, Germany

⁴ German-Dutch Wind Tunnels, 37073 Göttingen, Germany

The focus of this work is to assess the suitability of the BOS method for low compressibility flow measurements by visualising cylinder flow phenomena at low Mach numbers, which has not been shown before. The retroreflective BOS method, described by Heineck et al. (2010), has been applied in the present study due to the limited optical access of the pressurised wind tunnel.

2 Theory

The working principle of BOS is the analysis of light deflections due to changes of the refraction index, which in most applications are caused by density gradients in the investigated fluid. A measurement image of the flow with a background pattern is compared to an undisturbed reference image whereby the resulting apparent shift of the background pattern is related to the change of the refraction index. The refraction index n is coupled to the density ρ via the Gladstone–Dale constant k . According to Oertel (1989) the relationship between n and ρ is defined for high pressures as:

$$\frac{n^2 - 1}{n^2 + 2} = \frac{2}{3}k\rho. \tag{1}$$

This can be simplified to the commonly used form when $(n - 1) \ll 1$:

$$n - 1 = k\rho \tag{2}$$

For the current investigation the simplification results in a maximum error of 0.25% for $(n - 1)$, which is considered an acceptable inaccuracy.

The angle ε by which incident light rays are deflected depends on the Gladstone–Dale constant k , the refraction index n_0 and the density gradient normal to the line of sight, see Settles (2006). The coordinate system used in the present investigation is shown in Fig. 1. The line of sight of the BOS measurements was parallel to the cylinder axis z . For two-dimensional density gradient fields (constant gradients along the line of sight) the deflection angle can be determined by integrating over the axial extent of the density gradient:

$$\varepsilon_x = \frac{k}{n_0} \frac{\partial \rho}{\partial x} \int dz \tag{3}$$

where the coordinate direction x stands either for the radial coordinate r or the circumferential coordinate $r\varphi$ in the current setup. The small deflection angle results in an apparent shift of the background pattern:

$$\frac{dx}{dz} = \tan \varepsilon \approx \varepsilon. \tag{4}$$

For a more thorough discussion of the working principle of schlieren imaging in general, see Settles (2006), or

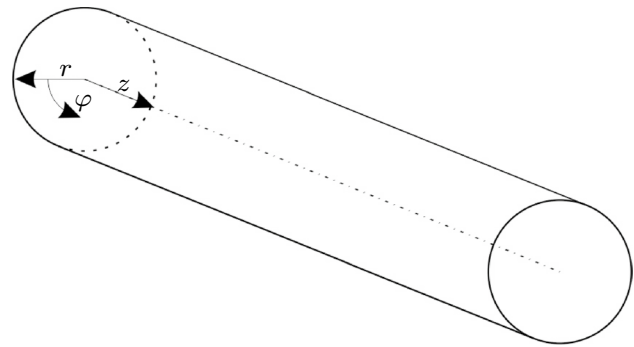


Fig. 1 Polar coordinate system used in the current investigation

refer to Venkatakrishnan and Meier (2004) for a discussion of the BOS method.

In high pressure wind tunnels, similarity of the Reynolds number can be achieved by either varying the static pressure or the velocity. It is essential for the schlieren investigations to determine which of these two parameters governs the strength and visibility of the density gradients. Therefore, an estimation of the expected shift of the background pattern caused by the flow around a cylinder is derived.

The density gradients of the flow around a cylinder can be estimated from potential theory. Assuming the dimensionless pressure field represented by the pressure coefficient c_p to follow potential theory in the first part of the cylinder ($\varphi < 90^\circ$), the corresponding density field can be derived. The pressure coefficient is defined as the difference between the pressure p at a given position in the flow and the reference pressure in the freestream p_∞ related to the stagnation pressure $q_\infty = \frac{1}{2}\rho_\infty u_\infty^2$:

$$c_p = \frac{p - p_\infty}{q_\infty} = \frac{p - p_\infty}{\frac{1}{2}\rho_\infty u_\infty^2}. \tag{5}$$

Here, ρ and u denote the density and velocity, respectively, and the index ∞ indicates freestream values. The density is nondimensionalised with its freestream value:

$$\rho^* = \frac{\rho}{\rho_\infty}. \tag{6}$$

In a compressible, inviscid, and isentropic flow, as it is found upstream of the cylinder where turbulence is negligible, the pressure and density changes are coupled:

$$\frac{dp}{d\rho} = c^2 = \gamma RT \approx c_\infty^2 = \gamma RT_\infty. \tag{7}$$

Here, c is the speed of sound, γ is the heat capacity ratio, R is the specific gas constant, and T is the temperature. The influence of a moderate temperature change

on the speed of sound is neglected here. The density gradients are therefore estimated from Eq. (7) using the freestream value T_∞ for the temperature.

Making this equation dimensionless by introducing Eqs. (5) and (6) we obtain,

$$\frac{dc_p}{d\varphi^*} \approx 2 \frac{c_\infty^2}{u_\infty^2} = \frac{2}{M_\infty^2} \tag{8}$$

where $M = u/c$ is the Mach number. Integration of this equation with the boundary condition in the far stream ($c_p = 0, \varphi^* = 1$) yields

$$c_p \approx \frac{2}{M_\infty^2} (\varphi^* - 1). \tag{9}$$

According to potential theory, the pressure coefficient on the cylinder surface is related to the angular surface coordinate φ (the incident flow coming from $\varphi = 0^\circ$)

$$c_{p,pot} = 1 - 4 \sin^2(\varphi). \tag{10}$$

The equivalent equation for the dimensionless density can be obtained by introduction of Eq. (9) into Eq. (10) and reformulation

$$\varphi_{pot}^* \approx \frac{M_\infty^2}{2} - 2M_\infty^2 \sin^2(\varphi) + 1. \tag{11}$$

From the distribution, the gradient in circumferential direction can easily be calculated

$$\frac{d\varphi_{pot}^*}{d\varphi} \approx -4M_\infty^2 \times \sin(\varphi) \cos(\varphi), \tag{12}$$

and with that the gradient of the absolute value of the density becomes

$$\begin{aligned} \frac{d\varrho_{pot}}{d\varphi} &\approx \frac{-4\varrho_\infty u_\infty^2}{c_\infty^2} \sin(\varphi) \cos(\varphi) \\ &= \frac{-8q_\infty}{c_\infty^2} \sin(\varphi) \cos(\varphi). \end{aligned} \tag{13}$$

From Eqs. (3) and (4) the measurable shift in circumferential direction $\Delta\varphi$ can be determined by integration along the line of sight (Δz) with $x: = r\varphi$

$$\Delta\varphi \approx \frac{\Delta z^2}{2r^2} \frac{k}{n_0} \frac{\partial\varrho}{\partial\varphi}. \tag{14}$$

For the potential flow, the circumferential shift is derived from Eqs. (13) and (14):

$$\Delta\varphi_{pot} \approx -4 \frac{\Delta z^2}{r^2} \frac{k}{n_0} \frac{q_\infty}{c_\infty^2} \sin(\varphi) \cos(\varphi). \tag{15}$$

The peak value of $\Delta\varphi_{pot}$ in the range between $\varphi = 0^\circ$ and 90° is reached at $\varphi = 45^\circ$:

$$\Delta\varphi_{pot} \Big|_{\varphi=45^\circ} \approx -2 \frac{\Delta z^2}{r^2} \frac{k}{n_0} \frac{q_\infty}{c_\infty^2} = -\frac{\Delta z^2}{r^2} \frac{k\varrho_\infty}{n_0} M_\infty^2. \tag{16}$$

From this it can be concluded, that the maximum shift is influenced by the geometric parameter $\Delta z^2/r^2$, the parameter $k\varrho_\infty/n_0$, and the squared Mach number M_∞^2 representing a quadratic influence of the inflow velocity. The parameter $k\varrho_\infty/n_0$ can further be approximated as $k\varrho_\infty$ assuming a linear influence of the ambient density. Thus, for a given Reynolds number, a higher sensitivity of the BOS system is obtained for lower ambient pressure and a corresponding higher inlet velocity.

3 Experimental setup

3.1 Wind tunnel

Experiments were carried out in the closed return high pressure wind tunnel of the German-Dutch-Wind Tunnels (DNW) in Göttingen, Germany. It was operated at pressures between 0.1 and 6 MPa at ambient temperature. The temperature was controlled by external spray cooling, especially at high Reynolds numbers. The respective freestream velocities varied from 10 to 31 m/s with a freestream turbulence intensity of around 1%.

An aluminium cylinder with a diameter of 0.06 m was placed horizontally in the test section, which has a square cross section of 0.6 m width. The cylinder extended over the entire width of the test section and had a smooth surface (roughness average $R_a < 0.6 \mu\text{m}$). A sketch of the setup is shown in Fig. 2.

3.2 Experimental conditions

In total, eight different settings (cases A to H) ranging from $Re = 0.1 \times 10^6$ at atmospheric boundary conditions to $Re = 6.0 \times 10^6$ at $p = 5.6 \text{ MPa}$ have been investigated. The respective values of the pressure, Reynolds number, freestream velocity, stagnation pressure, Mach number, and freestream temperature are given in Table 1. For all of these settings, the Mach number is below 0.1 and the flow can classically be considered as incompressible. The stagnation pressure ranges from 0.385 to 30.5 kPa resulting in an expected range of schlieren strength of almost two orders of magnitude. The last column of Table 1 shows the expected maximum angular displacement in the circumferential direction, as determined from Eq. (16) with $\Delta z = 0.6 \text{ m}$ and $r = 0.03 \text{ m}$ for the investigated cylinder geometry.

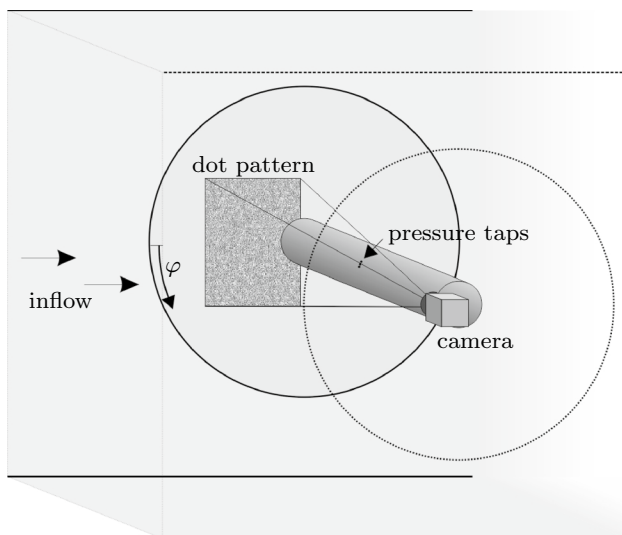


Fig. 2 Wind tunnel setup showing the arrangement of the camera with the cylinder and the background dot pattern

3.3 Pressure taps

The model cylinder was equipped with three pressure taps of 0.3 mm diameter at its half-span location, see Fig. 2. One tap was aligned with the central symmetry plane of the camera and the other two in flow direction 10° before and after that, respectively, see also Fig. 2. The taps were connected to a 64-port, digital, temperature-compensated, electronic pressure scanner with a range of ± 103 kPa differential. The acquisition frequency of the system was approximately 100 Hz. Pressure data were acquired and averaged over a period of 20 s for each data point. Specific calibration was performed for each tunnel pressure level, leading to a final accuracy of the pressure measurements of $\pm 0.5\%$.

3.4 BOS setup

The BOS setup was aligned with the cylinder to allow for an investigation of the density gradients perpendicular to

the cylinder axis. A CMOS (complementary metal-oxide semiconductor) camera was placed in a pressurised housing that was attached to one of the test section walls directly adjacent to the cylinder (see Fig. 2). The axial distance between the camera lens and the wind tunnel wall was approximately 20 mm. The used GigE (gigabit ethernet) camera has a resolution of $640 \text{ px} \times 480 \text{ px}$ and a pixel size of $4.8 \mu\text{m}$. An optical window (borosilicate glass) allowed for the observation of the flow field close to the cylinder surface. A typical endocentric camera lens with a focal length of 12 mm and an f-number of 16 was used here, resulting in an observation angle of 14.6° in the camera horizontal axis. Due to this slightly diverging observation angle, focus of the investigation was put on a small region in direct proximity of the cylinder surface, where the angle between the cylinder axis and the line of sight was below 5° . To capture the average flow field around the entire circumference of the cylinder, the cylinder, the camera, and the background were mounted on a turntable, which allowed the entire setup to be rotated around the cylinder axis. For the current investigation, the setup was rotated in 5° steps between the upstream ($\varphi = 0^\circ$) and the downstream ($\varphi = 180^\circ$) side of the flow.

A random dot pattern was printed on a retroreflective foil and applied to the wind tunnel wall opposite to the camera. The dots of the pattern are 0.7 mm in diameter with a density of 86 dots/cm^2 . This background was illuminated with two light emitting diode (LED) arrays with a maximum light output of 1950 lumen each. The LEDs were mounted in the turntable with a distance of 52 mm from the camera axis and were equipped with lenses which focussed their light into 15° cones.

The resolution of the camera in the background is approximately 3.89 px/mm . The cylinder-parallel line of sight is located 0.28 mm from the cylinder surface. For the angular coordinate, this resolution is equivalent to approximately $2.04 \text{ px}/^\circ$ at the cylinder surface.

Taking the velocity distribution from potential theory, the boundary layer thickness can be estimated with an integral method as described by Schlichting and Gersten

Table 1 Settings of test parameters investigated in the current study together with the maximum expected shift according to Eq. (16)

Case	$Re (\times 10^6)$	p_∞ (MPa)	u_∞ (m/s)	q_∞ (kPa)	M_∞ (-)	T_∞ (K)	$\Delta\varphi_{\text{pot}} _{\varphi=45^\circ} (\times 10^{-3})$
A	0.10	0.10	25.4	0.385	0.073	298	-0.59
B	0.25	0.25	26.1	0.998	0.075	300	-1.5
C	0.50	0.50	26.3	2.02	0.076	301	-3.1
D	1.0	1.0	26.8	4.15	0.077	304	-6.2
E	2.0	2.0	26.9	8.40	0.077	303	-13
F	2.0	5.6	10.0	3.24	0.029	304	-4.8
G	4.0	5.6	20.3	13.2	0.058	305	-19
H	6.0	5.6	30.9	30.5	0.087	310	-44

(2006). The resulting maximum thickness for the laminar boundary layer section ranges from 0.03 mm at the highest Reynolds number investigated up to 0.4 mm at the lowest Reynolds number. For the lower Reynolds numbers of the cases A–C, these values are in the same order of magnitude as the first radial point of the BOS analysis.

For every investigated setting, 500 reference images have been taken at an angular position of 0° with the wind tunnel running at approximately 2 m/s. This slow flow was necessary to suppress inevitable thermal disturbances at the cylinder surface, which occurred due to minor differences between the fluid and the cylinder temperature.

At every measurement angle, a total of 1000 images had been acquired with a frame rate of 50 Hz. The frame rate was chosen for the total recording time to match the measurement and averaging time of the flow and pressure measurements. The observed vortex shedding frequency varied between 25 and 300 Hz, depending on the flow conditions. The shedding frequency was found to always differ from the image frame rate of 50 Hz, resulting in a phase-variable image acquisition, as required for obtaining the true average density field.

3.5 Image analysis

Several processing steps are necessary to get from the raw images to the density gradient field. Before starting the analysis, the reference images are averaged to filter out eventual disturbances in a single reference image. Alternatively, the mean offset of a single background image can

be determined and subtracted as described in Stadler et al. (2017). However, as fluctuations between the reference images have been negligible in the current investigation, the simpler averaging of the reference image was selected here. An image registration or alignment of the reference image and the image under test conditions was not used in the current analysis.

The individual processing steps of the data analysis are outlined in Fig. 3. A sample raw image is depicted in Fig. 3a showing the field of view of approximately $164 \text{ mm} \times 123 \text{ mm}$ on the background. The dark shape at the upper image border is a part of the cylinder which is located about 20 mm away from the camera lens and thus out of focus. The extent of the corresponding blurred region in the images is estimated after Trommershäuser et al. (2011). The blur affects the background intensity in a region of up to 46 px above the cylinder surface and is constant over all images. This inhomogeneous illumination has no significant effect on the image analysis due to intensity normalisation prior to cross correlation.

The cylinder-parallel line of sight is located about 1 px from the cylinder surface. Consequently, a small part of the cylinder surface close to the background shows reflections of the background pattern that have to be masked during the evaluation.

In the first processing step, the displacements of the recorded background pattern between the averaged reference image and a single flow image were determined with a multi-grid cross-correlation algorithm realised in the

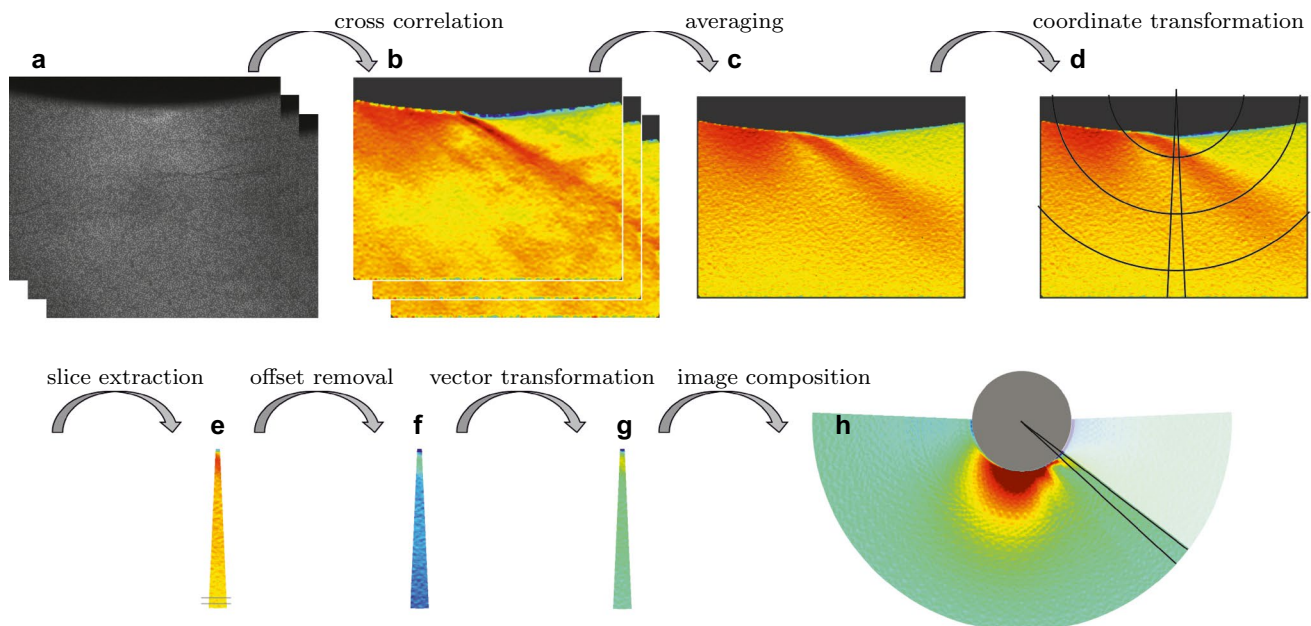


Fig. 3 Illustration of the individual image processing steps employed in the current analysis starting from the raw image (a) and resulting in the composite displacement fields (h). A detailed description of the individual steps is given in Sect. 3.5

Fig. 4 Mean pixel displacements in radial (*left*) and circumferential (*right*) direction. The *top* images are for $Re = 0.1 \times 10^6$ and the *bottom* images are for $Re = 6.0 \times 10^6$. The complete description of the settings is given in Table 1

commercial PIV-software DAVIS 8.22 from LaVision. The initial interrogation window size in the analysis was $24 \text{ px} \times 24 \text{ px}$ with 50 % overlap, which was successively reduced to $8 \text{ px} \times 8 \text{ px}$ with 75 % overlap.

All 1000 individual displacement fields for each flow condition and measurement angle have been averaged to obtain the mean displacement of the respective setting. The Cartesian pixel coordinates have been transformed to polar coordinates originating on the axis of the cylinder. A circumferential segment of $\pm 2.5^\circ$ around the image centre has been extracted from the average image.

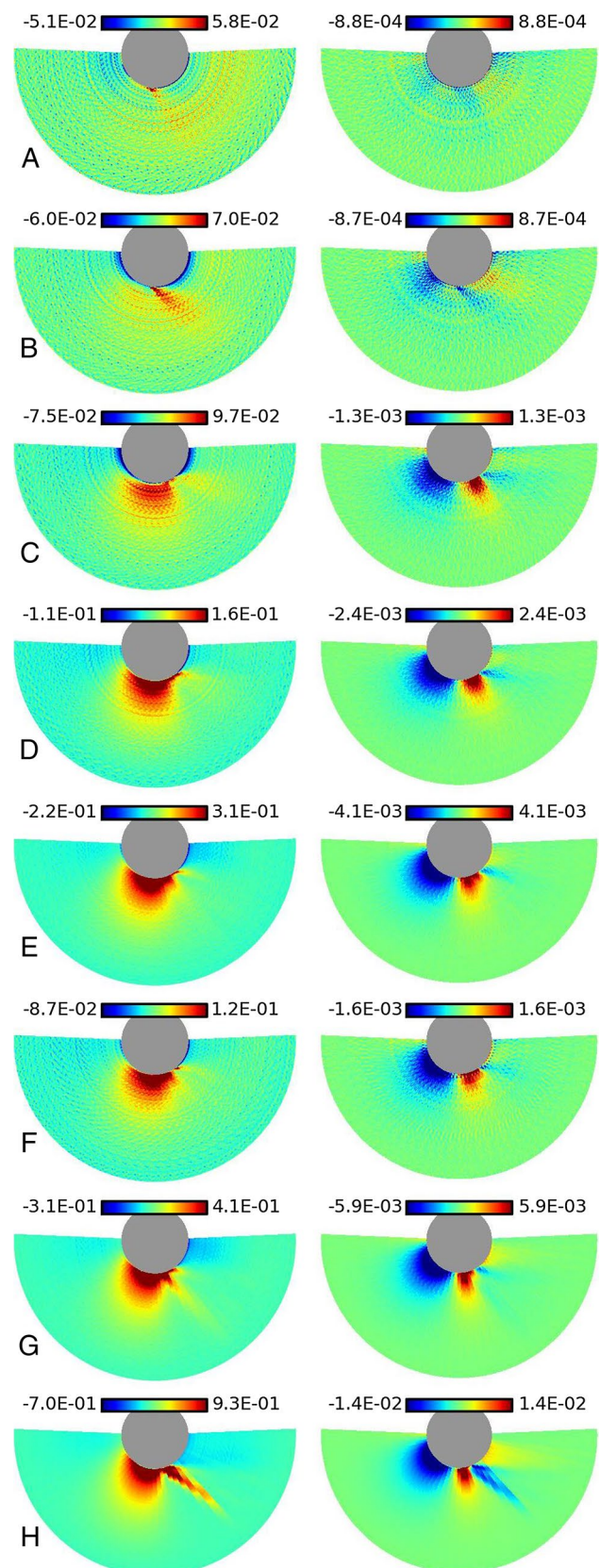
Since all images were analysed relative to the reference taken at 0° , a certain global offset occurred at angular positions different from 0° . This offset corresponds to an axial skew of the camera of below 0.025° , which is attributed to the plates of the turntable not being perfectly parallel. The offset caused by the relatively small camera misalignment is of similar order of magnitude as the investigated displacements for the first test cases and, therefore, had to be compensated for. For the current investigation it was found that the smallest error was introduced by enforcing an assumed zero displacement on the periphery of the images. The offset was therefore calculated by averaging the displacement values of six pixel rows close to the outer edge of the image, as shown in Fig. 3e.

These displacement fields have been transformed from Cartesian coordinates to polar coordinates (Fig. 3g) and finally a combined displacement field based on the offset-corrected 5° sections for each circumferential measurement position has been stitched together as shown in Fig. 3h.

4 Results

4.1 Pixel displacement fields

An overview of the measurement results corresponding to different pressure and flow velocity settings is given in Fig. 4. The 16 subfigures correspond to the 8 flow conditions A–H specified in Table 1 and depict the average radial (left column) and circumferential (right column) pixel displacement fields induced by the density gradients in the cylinder flow. The plots are individually scaled to show a range of ± 3 standard deviations around the respective mean value.



For increasing Reynolds number from A to H the overall pixel shift increases except for case F for which the Reynolds number has been the same as in case E but at a higher pressure. While in case A a characteristic flow structure can hardly be identified due to the low signal-to-noise ratio, visibility of the flow structures continuously increases up to the final flow condition H. The improvement of the signal-to-noise ratio is caused by roughly constant image noise in combination with a signal increase by one to two orders of magnitude between cases A and H.

In cases A and B a “jet”-like structure originates at around 80° in the radial displacement field. This structure is inclined in flow direction and extends about one third of the investigated radius. From case C on this “jet”-structure turns into a “bubble”, which is centred at around 80° in case C and slightly moves forward with higher Reynolds numbers.

In addition to the large “bubble” an additional “jet”-like structure appears in the radial displacement field which is faintly visible in case C at around 130° . For increasing Reynolds numbers, the displacement magnitude of this “jet” grows and surpasses the magnitude of the “bubble” in case H, while simultaneously appearing at earlier circumferential angles of down to 110° in case H.

Concurrent trends can be observed for the circumferential displacement component shown on the right side of Fig. 4. Again, in case A and B the displacement is barely distinguishable from the background noise and exhibits a noticeably different flow structure from that in cases C to H. From case C on a maximum negative pixel displacement occurs near the cylinder surface at about 30° – 50° , which is followed by a maximum positive displacement at 115° in case C and 95° in case H. A second negative displacement zone in the circumferential direction corresponds to the end of the “jet”-like structure seen in the radial displacement field.

It should be noted that cases E and F show the displacement fields at the same Reynolds number analysed at different pressure levels. As expected, the observed flow structures are similar but the signal-to-noise ratio in case F is reduced because of the lower stagnation pressure at the higher ambient pressure level.

4.2 Comparison to potential theory

When the density field is two-dimensional, i.e. the density does not change in the direction of the cylinder axis, the measured displacement field is equivalent to a density gradient field in regions where the camera line of sight is parallel to the cylinder axis. The fields can be converted by solving the discretised form of Eq. (14) for ρ . As a good approximation, the density field can be considered two-dimensional at least up to the separation point. The camera is positioned at the cylinder surface to ensure that the line of sight is parallel to the cylinder axis in direct proximity to

the cylinder surface. Thus, the circumferential density distribution can be estimated close to the cylinder surface (4 px from the surface).

The density estimation is compared to theoretical values in order to validate the underlying assumptions. Up to a certain point the density should follow potential theory. Since in potential theory the flow properties reach ambient conditions at $\varphi = 30^\circ$, integration of the density was started at this point.

For better comparison to the measured pressure distribution as well as to potential theory, the evaluated density estimation has been nondimensionalised and scaled with $2/M_\infty^2$ and thereby converted to a pressure coefficient according to Eq. (9). This trend is plotted together with the measured dimensionless pressure distribution in Fig. 5 for all flow conditions investigated in this study. In addition, the raw radial displacement is shown for the same radial pixel coordinate.

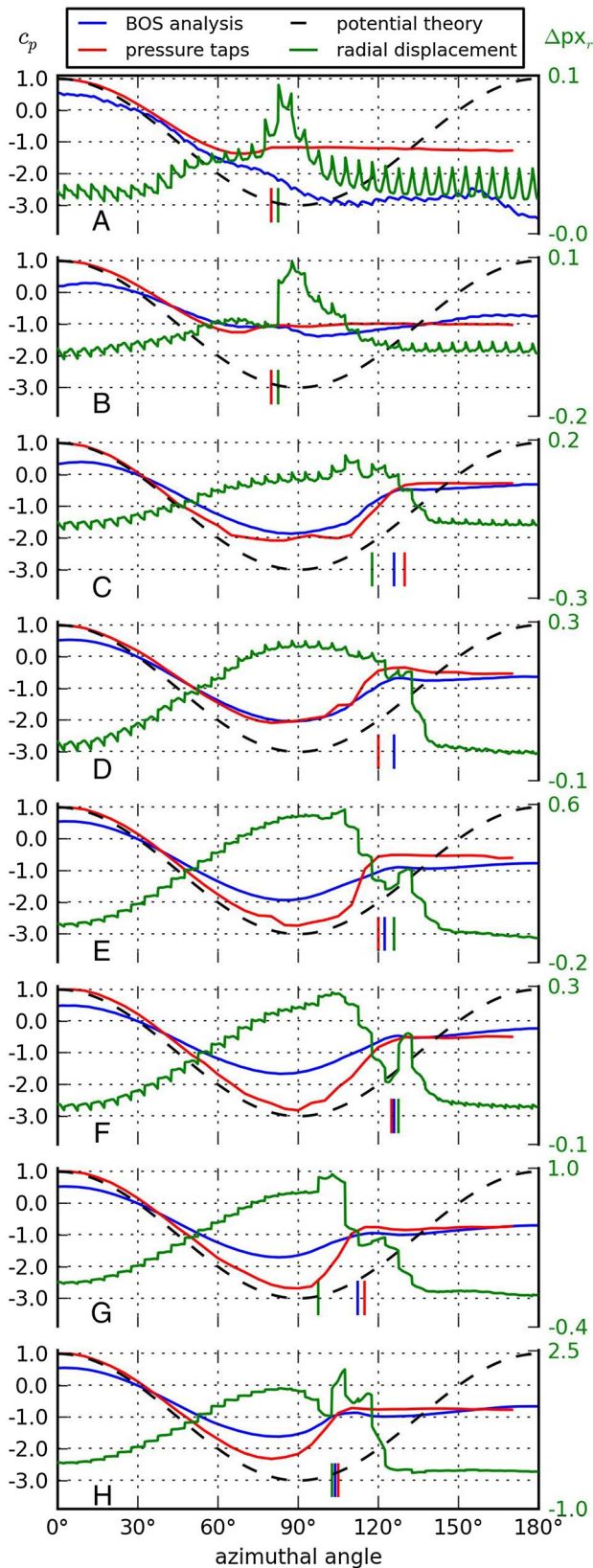
The measured surface pressure and integrated density exhibit very similar trends. Only for the very low Reynolds number in case A, where the signal-to-noise ratio is low and the general flow structure in Fig. 4 was hardly distinguishable, the trend of the integrated density deviates considerably from that of the surface pressure.

Both trends follow the potential theory curve at least up to an angle of $\varphi = 50^\circ$ and in some cases up to $\varphi = 110^\circ$. The theoretical minimum at $\varphi = 90^\circ$ is not fully reached. In cases C–H the pressure recovery is captured up to a point from which on the pressure coefficient stays almost constant at $c_p = -1$. This point is the separation point of the flow around the cylinder and it is recorded in both flow properties at a very similar position.

It is noted that the BOS analysis generally yields lower values than the respective pressure distribution and is thus also short of the theoretical value. It seems not to be scaled correctly as its value in the stagnation point $\varphi = 0^\circ$ is always below 1 and the value at $\varphi = 90^\circ$ is almost always above the value of the respective pressure distribution.

A certain difference can be seen between cases E and F at the same Reynolds number. The pressure recovery around 100° is quicker in case E at $p = 2.0$ MPa compared to case F at $p = 5.6$ MPa.

The radial displacement curves underline the description of the contourplots in Sect. 4.1. The “bubble”-regime is characterised by a continuous increase and decrease of the displacement magnitude, the “jet”-like structure is characterised by discontinuous jumps in the observed displacement. In cases A and B a continuous increase from $\varphi = 0^\circ$ to the onset of the “jet”-like structure at around $\varphi = 80^\circ$ can be seen highlighting the existence of a “bubble”-regime which could not be definitely identified in the contourplots. However, its magnitude is well below that of the “jet”-structure. From the distribution of case A the background noise can be estimated to be approximately 0.1 px.



◀ **Fig. 5** Comparison of BOS analysis and measured pressure distribution with potential theory. The *top image* is for $Re = 0.1 \times 10^6$ and the *bottom image* is for $Re = 6.0 \times 10^6$. The complete description of the settings is given in Table 1. The *short vertical lines* at the bottom of each image denote the separation point

4.3 Boundary layer separation

The separation point of the boundary layer can be deduced from the density and pressure fields depicted in Fig. 5. Separation occurs where the gradient in the circumferential direction switches from positive to zero. For the current analysis, these points have been identified directly from the graphs. They coincide well for cases C–H, but the evaluation fails for the density derived distribution in the first two cases where the signal-to-noise ratio is very low. However, in these two cases the “jet”-like structure was observed in the radial displacement field in Fig. 4. It can be seen that the starting point of this peak coincides with the separation point in the pressure field. Moreover, at the higher Reynolds numbers where the “jet”-like structure appeared after the “bubble”, the peak in the radial displacement also coincides with the separation point determined with either the BOS analysis or the pressure measurements.

The separation points determined with these three methods are indicated in Fig. 5 with short vertical lines. It should be noted, that in the current investigation the pressure was measured every 5° , whereas the density gradient is shown with a resolution of $2 \text{ px}/^\circ$. Thus, a certain offset between the evaluation methods is inevitable.

In Fig. 6 the separation angles evaluated for each investigated case are plotted over the Reynolds number together with literature values from Achenbach (1968). The general trends observed correspond well between the different current methods and literature values.

Up to $Re = 0.2 \times 10^6$, the flow belongs to the so-called pre-critical or subcritical regime with an early separation between 80° and 90° (see Zdravkovich 1997). From $Re = 0.5 \times 10^6$ on, the separation occurs at around 120° in the so-called critical regime and moves again to the front for $Re > 2.0 \times 10^6$ in the supercritical regime.

4.4 Standard deviation of displacement fields

A different means of analysing the time-resolved displacement data is to look at the standard deviation of the displacement fields. Figure 7 depicts the standard deviation around the mean values of the recorded 1000 individual images shown in Fig. 4.

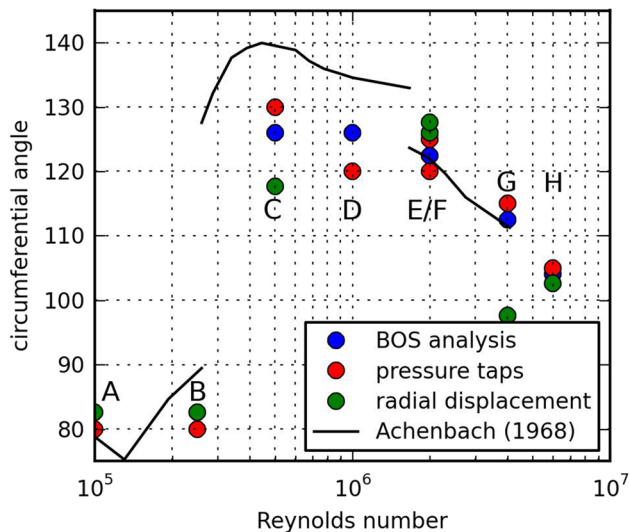


Fig. 6 Circumferential angle of the separation point over the Reynolds number as evaluated for the current experiments compared to Achenbach (1968)

The standard deviation graphs highlight regions with maximum intermittency, whereas steady parts of the displacement fields are filtered out. Most interesting are the first two cases where in the mean displacement fields almost no structure could be identified, but the standard deviation clearly shows zones of strong oscillations. The largest values of the standard deviation of the radial component seen on the left of Fig. 7 coincide with the appearance of the “jet”-like structures in the mean images (Fig. 4). In both directions, but more pronounced in the circumferential direction, the regime typically associated with the wake of the cylinder flow is characterised by high values of the standard deviation.

5 Discussion

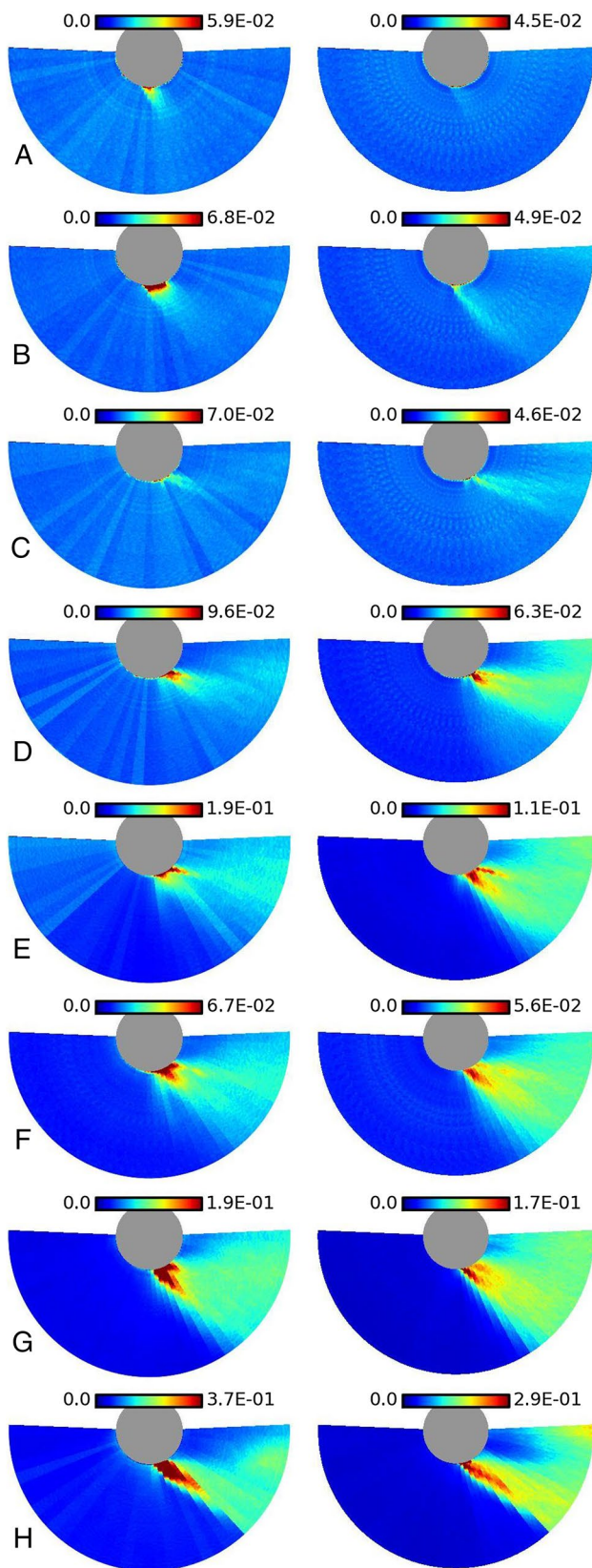
The presented measurement results in Fig. 4 give a good impression of the density gradient fields in the flow around circular cylinders. The increase in signal strength (magnitude of pixel displacement) corresponds well with the expected behaviour due to an increase of the stagnation pressure. Absolute values of the recorded pixel displacement in circumferential direction are also in accordance with the theoretical values given in the last column of Table 1.

In the mean displacement field of case A in Fig. 4, the noise exhibits a regular pattern which repeats in every 5° section. As all images of a given flow condition were correlated with the same mean reference image regardless of the circumferential position, this pattern is attributed to a noisy background image. This pattern is slightly shifted

and rotated according to the above mentioned skew of the camera axis so that it cannot simply be subtracted from the final image. The background noise is therefore close to constant for all cases and results in signal-to-noise ratios between approximately 2 at the lowest and 80 at the highest Reynolds number investigated. This background noise can be overcome with individual reference images for every observation angle. At the same time, a reduction of the image noise would improve the signal-to-noise ratio allowing for investigations at even lower stagnation pressures. Although the signal-to-noise ratio improves with the stagnation pressure, an upper limit for the application of BOS is postulated for large pixel displacements. For displacements above 1 px, the corresponding displacement vector cannot be attributed to a single pixel location anymore. Also, surfaces near large shifts and steep changes in the shift can cause errors due to the finite interrogation window size. The maximum evaluated pixel shift in the current study is 6 px in the circumferential direction. This is considered an acceptable value as the change of the gradient is smooth over the circumference.

It is noticeable that the composition of the displacement fields was conducted without any smoothing of the individual image slices, yet the 5° sections of the individual images blend well into each other. The small transitions that can be seen primarily in the “jet”-like structure at high Reynolds numbers can be attributed to the increasing inclination of the line of sight with increasing distance from the cylinder. A backtransformation of this perspective distortion has not been expedient since the backtransformation is very sensitive to input noise.

The trend of the integrated density shows an unrealistic behaviour in case A as it falls below the theoretical minimum which can be attributed to the low signal-to-noise ratio. In the other cases, the difference between the integrated density field and the trend from potential theory shown in Fig. 5 shows a systematic error as the absolute values are always too low. This underestimation is probably caused by various effects. First of all, the integration path is not exactly on but 4 px or about 1 mm away from the cylinder surface where the gradients obtained from potential theory are lower, too. In addition, the density gradients very close to the camera are out of focus and thus cause image blur. Another possible explanation is the offset removal during image composition. The offset value has been determined at the outer edge of the individual images assuming a zero displacement. Since in reality a minor displacement still prevails in this region, the offset value is overestimated leading to an underestimation of the gradient field. Moreover, due to the perspective distortion an additional uncertainty is superposed on the offset estimation. In future applications these effects can be addressed by



◀ **Fig. 7** Standard deviation of pixel displacements in radial (*left*) and circumferential (*right*) direction. The *top images* are for $Re = 0.1 \times 10^6$ and the *bottom images* are for $Re = 6.0 \times 10^6$. The complete description of the settings is given in Table 1

the above already mentioned individual background images for every observation angle and the use of telecentric camera lenses which in combination might significantly reduce the need for offset corrections. A minor systematic error might also be due to calibration errors of the optical setup. The setup affects primarily the background resolution (px/mm) and the apparent position of the cylinder axis in the recorded images. A variation of these parameters by $\pm 10\%$ resulted in only negligible quantitative changes of the evaluated gradients.

In accordance with Achenbach (1968), the plot of the separation points over the Reynolds number in Fig. 6 shows a discontinuous jump between the sub-critical (case A and B) and the critical regime in the same way as the plots of the displacement fields in Fig. 4 exhibit different flow structures. From the critical to the supercritical regime, the transition in both representations is continuous and smooth. The difference between the literature values and the current investigation in cases C and D could be caused by several effects like differences of the actual surface roughness, the wind tunnel blockage, or wind tunnel turbulence intensities. However, the congruence between pressure measurements and BOS analysis is more important for the focus of this study.

From comparison of the mean displacement fields in Fig. 4 and the standard deviation fields in Fig. 7, it becomes apparent that the so-called “bubbles” are stationary phenomena which are associated with the potential behaviour of the flow. Based on the high standard deviation levels, the circumferential position of the articulated “jet”-like structures moves back and forth. Consequently, it stands to reason that the actual separation point also moves back and forth over time. This can also be seen in Fig. 3b, c, where in the individual image the maximum value is in the “jet”-like structure whereas it appears to have moved to the “bubble” in front of it in the mean image.

While no direct physical interpretation of the standard deviation fields shown in Fig. 7 is apparent, these images on first sight clearly indicate the boundary layer separation as well as the extent of the fluctuating regime in the wake of the cylinder. As the standard deviation fields only highlight regions of strong intermittency, the actual separation points cannot be identified, only the extent of the region in which the separation point moves back and forth can be determined. The combination of mean and standard deviation plots is thus very helpful in the interpretation of the present data.

6 Conclusions and outlook

The presented results for the first time show the applicability of BOS for the investigation of density fields in high Reynolds number flows at low Mach numbers. It has been shown on a theoretical basis and verified experimentally that the strength of the recorded schlieren primarily scale with the stagnation pressure. For the current setup a sensitivity limit is reached at ambient conditions at $Re = 0.1 \times 10^6$ but ideas to further reduce this limit are presented.

Signal-to-noise ratios between 2 and 80, depending on the stagnation pressure, have been achieved. An improvement of the signal-to-noise ratio could be achieved by individual background images for every angle of observation. It is important to note that the signal noise in the current analysis is primarily caused by the image composition and not by the cross-correlation algorithm. Therefore, a further enhancement could be possible. An upper limit for the signal strength of the analysis is given by the fact that pixel shifts above 1 px cannot be ascribed to a single pixel coordinate leading to smearing effects in the spatial domain.

The measured displacement fields show characteristic flow structures which can be associated to the so-called subcritical, critical and supercritical flow regimes. With the integration of the measured density fields in the circumferential direction it is possible to identify the separation point non-intrusively. It coincides very well with concurrent pressure measurements. Furthermore, a comparison of the integrated density fields on the cylinder surface with potential theory shows good agreement.

A full quantitative analysis including the radial direction can be achieved by different approaches. For the available data, a backtransformation could be applied to compensate for the image distortion due to the viewing angle. Though, this density reconstruction is very sensitive to the signal noise. A better approach would be a setup with a telecentric lens or a parabolic mirror (Elsinga et al. 2004) to enable the investigation of cylinder-parallel light rays throughout the field of view. Furthermore, a full three dimensional tomographic reconstruction could be obtained by either using a setup with multiple cameras, as for example shown by Nicolas et al. (2015), or by observing the measurement volume with a single camera from different perspectives and repeating the experiments, as for example shown by Goldhahn and Seume (2007).

Combining the analysis of the mean displacement fields with the respective standard deviation fields gives additional information especially in the low signal-to-noise ratio cases. Here, the regime in which boundary layer separation occurs can clearly be identified in the standard deviation fields. Moreover, the extent of the wake flow can distinctly be seen in these fields.

In the current setup the first pixels outside the cylinder have been in the order of the boundary layer thickness. With a further enhancement of the image resolution and with a focus on the boundary layer, BOS could potentially be used to identify transition in the boundary layer. This could open new fields of applications for this measurement technique.

Acknowledgements The authors gratefully acknowledge the support from the entire team involved in the experimental campaign and especially Markus Löhr for the smooth operation of the wind tunnel. This work was carried out with financial support from the Ministry of Innovation, Science and Research of the State of North Rhine-Westphalia (MIWF NRW), Germany, under contract 323-2010-006 (Start-SF).

References

- Achenbach E (1968) Distribution of local pressure and skin friction around a circular cylinder in cross-flow up to $Re = 5 \cdot 10^6$. *J Fluid Mech* 34(04):625. doi:[10.1017/s0022112068002120](https://doi.org/10.1017/s0022112068002120)
- Bauknecht A, Merz CB, Raffel M, Landolt A, Meier AH (2014) Blade-tip vortex detection in maneuvering flight using the background-oriented schlieren technique. *J Aircr* 51(6):2005–2014. doi:[10.2514/1.c032672](https://doi.org/10.2514/1.c032672)
- Coutanceau M, Defaye JR (1991) Circular cylinder wake configurations: a flow visualization survey. *Appl Mech Rev* 44(6):255–305. doi:[10.1115/1.3119504](https://doi.org/10.1115/1.3119504)
- Dalziel SB, Hughes GO, Sutherland BR (2000) Whole-field density measurements by 'synthetic schlieren'. *Exp Fluids* 28:322–335. doi:[10.1007/s003480050391](https://doi.org/10.1007/s003480050391)
- Elsinga G, Van Oudheusden B, Scarano F, Watt D (2004) Assessment and application of quantitative schlieren methods: calibrated color schlieren and background oriented schlieren. *Exp Fluids* 36(2):309–325. doi:[10.1007/s00348-003-0724-8](https://doi.org/10.1007/s00348-003-0724-8)
- Goldhahn E, Seume J (2007) The background oriented schlieren technique: sensitivity, accuracy, resolution and application to a three-dimensional density field. *Exp Fluids* 43:241–249. doi:[10.1007/s00348-007-0331-1](https://doi.org/10.1007/s00348-007-0331-1)
- Heineck JT, Schairer ET, Walker LA, Kushner LK (2010) Retroreflective background oriented schlieren (RBOS). In: 14th International Symposium on Flow Visualization
- Kakade AA, Singh SK, Panigrahi PK, Muralidhar K (2010) Schlieren investigation of the square cylinder wake: Joint influence of buoyancy and orientation. *Phys Fluids* 22(5):054,107. doi:[10.1063/1.3415228](https://doi.org/10.1063/1.3415228)
- Kindler K, Goldhahn E, Leopold F, Raffel M (2007) Recent developments in background oriented schlieren methods for rotor blade tip vortex measurements. *Exp Fluids* 43:233–240. doi:[10.1007/s00348-007-0328-9](https://doi.org/10.1007/s00348-007-0328-9)
- Nicolas F, Todoroff V, Plyer A, Besnerais GL, Donjat D, Micheli F, Champagnat F, Cornic P, Sant YL (2015) A direct approach for instantaneous 3D density field reconstruction from background-oriented schlieren (BOS) measurements. *Exp Fluids*. doi:[10.1007/s00348-015-2100-x](https://doi.org/10.1007/s00348-015-2100-x)
- Oertel H (1989) *Optische Strömungsmesstechnik*. Braun-Verlag. doi:[10.1007/978-3-642-51755-6](https://doi.org/10.1007/978-3-642-51755-6)
- Raffel M (2015) Background-oriented schlieren (BOS) techniques. *Exp Fluids* 56(3):1–17. doi:[10.1007/s00348-015-1927-5](https://doi.org/10.1007/s00348-015-1927-5)
- Raffel M, Richard H, Meier GEA (2000) On the applicability of background oriented optical tomography for large scale aerodynamic investigations. *Exp Fluids* 28(5):477–481. doi:[10.1007/s003480050408](https://doi.org/10.1007/s003480050408)

- Rodriguez O (1984) The circular cylinder in subsonic and transonic flow. *AIAA J* 22(12):1713–1718. doi:[10.2514/3.8842](https://doi.org/10.2514/3.8842)
- Schlichting H, Gersten K (2006) *Grenzschicht-Theorie*. Springer. doi:[10.1007/978-3-662-07554-8](https://doi.org/10.1007/978-3-662-07554-8)
- Settles GS (2006) *Schlieren and Shadowgraph Techniques*. ISBN: 10 3-540-66155-7. Springer Berlin/Heidelberg/New York
- Stadler H, Flesch R, Maldonado D (2017) On the influence of wind on cavity receivers for solar power towers: flow visualisation by means of background oriented schlieren imaging. *Appl Thermal Eng* 113:1381–1385. doi:[10.1016/j.applthermaleng.2016.11.099](https://doi.org/10.1016/j.applthermaleng.2016.11.099)
- Tokgoz S, Geisler R, van Bokhoven LJA, Wieneke B (2012) Temperature and velocity measurements in a fluid layer using background-oriented schlieren and PIV methods. *Measure Sci Technol* 23(11):115,302. doi:[10.1088/0957-0233/23/11/115302](https://doi.org/10.1088/0957-0233/23/11/115302)
- Trommershäuser J, Kording K, Landy M (2011) *Sensory Cue Integration*. Computational neuroscience. Oxford University Press. doi:[10.1093/acprof:oso/9780195387247.001.0001](https://doi.org/10.1093/acprof:oso/9780195387247.001.0001)
- van Hinsberg NP, Rösgen T (2014) Density measurements using near-field background-oriented schlieren. *Exp Fluids* 55(4):1720. doi:[10.1007/s00348-014-1720-x](https://doi.org/10.1007/s00348-014-1720-x)
- Venkatakrisnan L, Meier GEA (2004) Density measurements using the background oriented schlieren technique. *Exp Fluids* 37:237–247. doi:[10.1007/s00348-004-0807-1](https://doi.org/10.1007/s00348-004-0807-1)
- Zdravkovich M (1997) *Flow around circular cylinders: Volume I: Fundamentals*. Oxford University Press, New York. doi:[10.1115/1:2819655](https://doi.org/10.1115/1:2819655)